

Ag-AgO nanostructures on glass substrates by solid-state dewetting: From extended to localized surface plasmons

A. Serrano, O. Llorca-Hernando, A. del Campo, F. Rubio-Marcos, O. Rodríguez de la Fuente, J. F. Fernández, and M. A. García

Citation: *Journal of Applied Physics* **124**, 133103 (2018); doi: 10.1063/1.5049651

View online: <https://doi.org/10.1063/1.5049651>

View Table of Contents: <http://aip.scitation.org/toc/jap/124/13>

Published by the *American Institute of Physics*

Articles you may be interested in

[Effect of boron addition in modulating the optoelectronic properties of undoped and Al-doped ZnO thin films](#)
Journal of Applied Physics **124**, 135103 (2018); 10.1063/1.5046188

[Tailoring nanostructured surfaces with plasmonic/magnetic multifunctional response](#)
Applied Physics Letters **113**, 101908 (2018); 10.1063/1.5044697

[Morphology dependent resonance modes in highly porous TiO₂ microspheres](#)
Journal of Applied Physics **124**, 133102 (2018); 10.1063/1.5046488

[Thermally stimulated nonlinear vibration of rectangular single-layered black phosphorus](#)
Journal of Applied Physics **124**, 135101 (2018); 10.1063/1.5047584

[Influence of bulk and interfacial properties on shock compression of metal powders. I. Interaction of a pair of particles](#)
Journal of Applied Physics **124**, 134903 (2018); 10.1063/1.5030212

[Temperature dependent photoluminescence of anatase and rutile TiO₂ single crystals: Polaron and self-trapped exciton formation](#)
Journal of Applied Physics **124**, 133104 (2018); 10.1063/1.5043144

Ultra High Performance SDD Detectors



See all our XRF Solutions

Ag-AgO nanostructures on glass substrates by solid-state dewetting: From extended to localized surface plasmons

A. Serrano,^{1,2,a)} O. Llorca-Hernando,^{1,2} A. del Campo,¹ F. Rubio-Marcos,¹ O. Rodríguez de la Fuente,^{2,3} J. F. Fernández,¹ and M. A. García^{1,3}

¹*Instituto de Cerámica y Vidrio, Consejo Superior de Investigaciones Científicas, 28049 Madrid, Spain*

²*Dpto. de Física de Materiales, Universidad Complutense de Madrid, 28040 Madrid, Spain*

³*Instituto de Magnetismo Aplicado "Salvador Velayos", Universidad Complutense de Madrid, 28230 Madrid, Spain*

(Received 24 July 2018; accepted 10 September 2018; published online 3 October 2018)

We present here a study on the modification of morphological and plasmonic properties of Ag thin films deposited on glass substrates upon annealing in air at different temperatures. Initially, Ag films are continuous and exhibit extended surface plasmons with a resonant absorbance that depends on the film thickness. The dewetting process promotes the formation of nanoparticles with different sizes, shapes, and agglomerations states, besides a partial oxidation from Ag to AgO at surface level. The final Ag-AgO nanostructures are dependent on the annealing temperature and initial film thickness. The optical properties evolve from those typical of metallic films with high reflectivity and extended surface plasmon resonance toward localized surface plasmons characteristic of nanoparticles. The optical evolution and the final plasmonic response are evaluated according to the morphological and structural features of nanostructures. *Published by AIP Publishing.*

<https://doi.org/10.1063/1.5049651>

I. INTRODUCTION

Silver and silver oxide nanostructures in the form of thin films or nanoparticles (NPs) are interesting for both fundamental and applied purposes. The electronic configuration of Ag yields a very weak damping of the conduction electrons leading to notable optical properties. For example, Ag films are ideal for the fabrication of optical mirrors exhibiting a larger reflectivity than any other metal in the spectral range from 400 nm to the full IR region.¹ They also exhibit very intense extended surface plasmon resonance (ESPR) with a local amplification of the electric field of the light up to 80 times the incident light intensity.² Silver oxide films are potential candidates as electrode materials for supercapacitor applications due to their conductivity being significantly larger than other transition metal oxides.³ Ag NPs exhibit the most intense localized surface plasmon resonance (LSPR) that make them useful for biomarkers, photovoltaics, or surface-enhanced Raman spectroscopy (SERS).^{4–8} In addition, silver and silver oxide NPs can be used for antibacterial and catalytic applications.^{9–12} Even combined NPs-film systems such as the NPs-film-gap configuration based on Ag are also quite attractive since they can be adopted as an interesting tool in the typical analytical fields, offering high near-field enhancements for SERS or other plasmonic sensing.^{13,14} Consequently, the control of Ag nanostructures in the whole range from continuous thin films to NPs results quite appealingly in a large number of fields.

A well-known method to transform a noble metal film into NPs is the solid-state dewetting process, where annealed metallic thin films dewet to form islands.^{15,16} During the transformation, a series of modifications in metal films are induced: formation of hillocks or strain-free extrusions, growth of holes within the film, and agglomeration of islands leading to a discrete structure.^{17–22} This manufacturing process allows covering the whole path between a continuous film and three-dimensional nanostructures, and therefore, tuning the morphology and the optical features such as surface plasmons (SPs) to optimize a particular property. The fabrication of Ag nanostructures by thermal annealing of thin films has been reported in diverse works controlling parameters such as the annealing temperature, the annealing time, and the deposition amount, evaluating even the final SERS response.^{19,20,23,24}

In a previous work, we analyzed the morphological and optical transitions from continuous films to discrete nanostructures for the case of Au films treated thermally at different temperatures.²¹ Here, we extend the study to Ag with the highest extinction cross section coefficient associated with the excitation of SPs and showing SERS enhancement factors of 10^5 .^{2,25,26} Moreover, the fact that Ag can suffer some degree of oxidation upon annealing in air leads to a richer phenomenology in the plasmonic evolution that is analyzed in the present manuscript.

II. EXPERIMENTAL METHODS

Ag films were deposited onto sodalime glass substrates by electron-beam evaporation with a MANTIS QUAD-EC evaporator mounted on a home-made vacuum chamber. Prior to deposition, sodalime substrates were cleaned using soap and water and then dried with dry air flux. Ag films were grown using Ag wire (99.99% purity, 0.25 mm diameter),

^{a)} Author to whom correspondence should be addressed: aida.serrano@icv.csic.es. Tel.: +34 91 735 58 40. Fax: +34 91 735 58 43. ORCID: 0000-0002-6162-0014.

which was placed onto a Mo crucible. The wire was initially melted prior to the evaporation. Substrates were placed at 15 cm from the evaporator. The base pressure during evaporation was 10^{-6} Torr. Samples with thicknesses ranging from 10 to 50 nm were obtained by varying the evaporation time. Ag film thickness was controlled by a quartz crystal microbalance which was previously calibrated using X-ray reflectometry.

The thickness of the thin films was also determined for simulating extended surface plasmon (ESP) curves of as-grown Ag films by using the software Winspall version 3.02, a freeware to calculate and simulate SPR spectra with great accuracy.²⁷ This code is based on the Fresnel equations, including the correction of both reflection and refraction of the coupling prism. Fits were performed using 500 iterations, with the Ag film thickness being a free parameter and fixing the dielectric permittivity to $\epsilon_1 = -18.295$ and $\epsilon_2 = 0.48085$ (at $\lambda = 633$ nm, according to Johnson and Christy²⁸). Table I shows the nominal and calculated thicknesses of as-grown Ag films selected.

Thermal annealing process of Ag films was performed in air in three steps: (a) an initial stage of 2 h where sample temperature was gradually increased from room temperature (RT) to the target temperature, (b) 10 min at constant temperature, and (c) a last cooling stage where the temperature gradually decreased until the sample reached RT. The target temperatures were 300 °C, 400 °C, and 500 °C.

The morphology of samples was analyzed by scanning electron microscopy (SEM), confocal optical microscopy (COM), and atomic force microscopy (AFM) at RT. SEM images were taken with an S-4700 Hitachi instrument at 20 kV, and COM and AFM images were obtained with a WITec ALPHA 300RA, where the AFM is coupled to the confocal microscope. COM images were measured in reflected mode, while the AFM images were taken in non-contact mode and using silicon tips (with a resonant frequency of 200–300 kHz). Under the best measurement conditions, the optical resolution of the confocal microscope is about 350 nm. The morphological features of samples were examined by using the software ImageJ. Raman measurements were collected using the confocal Raman microscope (CRM) WITec ALPHA 300RA. The measurements were performed at RT with a Nd:YAG laser (532 nm) linearly polarized. Raman spectra were recorded in the spectral range 0–1100 cm^{-1} . In order to prevent any damage to the samples, laser excitation power was fixed at 0.4 mW. Collected spectra were analyzed by using WITec Control Plus software.

ESPR was measured in the attenuated total reflectance (ATR) mode in Kretschmann-Raether configuration with a

home-made device described elsewhere.^{21,22} Optical absorption spectra in transmission mode were collected with an UV–VIS–NIR Shimadzu 3100 double-beam spectrophotometer equipped with an integrating sphere. Spectra were recorded at RT from 200 to 800 nm with 0.5 nm spectral resolution.

III. RESULTS AND DISCUSSION

A. Morphological properties

Figure 1 shows the SEM images for samples with three different initial thicknesses. As-grown samples form a continuous polycrystalline film formed by grains with a size up to 200 nm irrespective of the film thickness.

Annealing in air induces the formation of holes, their percolation, and appearance of elongated islands that finally achieve rounded shape, in agreement with the previous studies.^{17–22,29} The process is completed at a temperature that depends on the initial film thickness: the thicker the initial film, the larger the annealing temperature required to complete the process. A representative scheme of the solid-state dewetting mechanism for a Ag film depending on the annealing temperature and the film thickness is presented in Figs. 1(m) and 2(e), respectively.

The morphological analysis of the nanostructures was completed by using COM and AFM, which confirmed the morphology and sizes provided by SEM, offering additional information about height distribution of the islands. Examples are shown in Fig. 2 for samples A and C annealed at 300 °C.

Noble metal thin films grown on oxide substrates exhibit a Volmer-Weber growth, and their morphological modifications upon annealing have been studied for a long time.^{21,29–32} When increasing the temperature, the difference in the thermal expansion coefficient between the substrate and the metallic film induces mechanical interface stress that increases the surface and interfacial energies. These energies are relieved by the activation of the dewetting process.¹⁵ Initially, the inhomogeneous stress distribution at the film/substrate interface promotes the formation of hillocks. Higher annealing temperature favors the appearance of holes and their subsequent growth due to the surface diffusion and grain growth.^{17,18,33} Finally, holes percolate leading to the formation of islands. For sufficiently high annealing temperatures, the surface coverage decreases and the islands tend to modify their shape becoming more rounded, in order to reduce their surface energy. It should be noted that at higher temperatures, the evolution of NPs can be affected, in addition to the surface diffusion, by the sublimation process that depends on the equilibrium vapor pressure increasing with the annealing and time temperature.²⁰ The final morphology of the nanostructures at the different stages of the process depends on the initial film thickness and the annealing conditions such as annealing time and temperature.

The formation and growth of holes is easier for thinner films because the amount of material that must be displaced to create a hole is lesser than for thicker films. Therefore, the process of formation of rounded nanostructures is achieved easily (i.e., at lower temperatures) for thin films as shown in Fig. 1. Actually, for thinner films, a larger number of holes

TABLE I. Nominal and calculated thickness of three selected Ag films deposited on sodalime substrates. Nominal thickness was obtained from a quartz crystal microbalance and calculated thickness was determined by using the software Winspall.

| Sample | Nominal thickness (nm) | Calculated thickness (nm) |
|--------|------------------------|---------------------------|
| A | 10 | 13 |
| B | 30 | 32 |
| C | 50 | 42 |

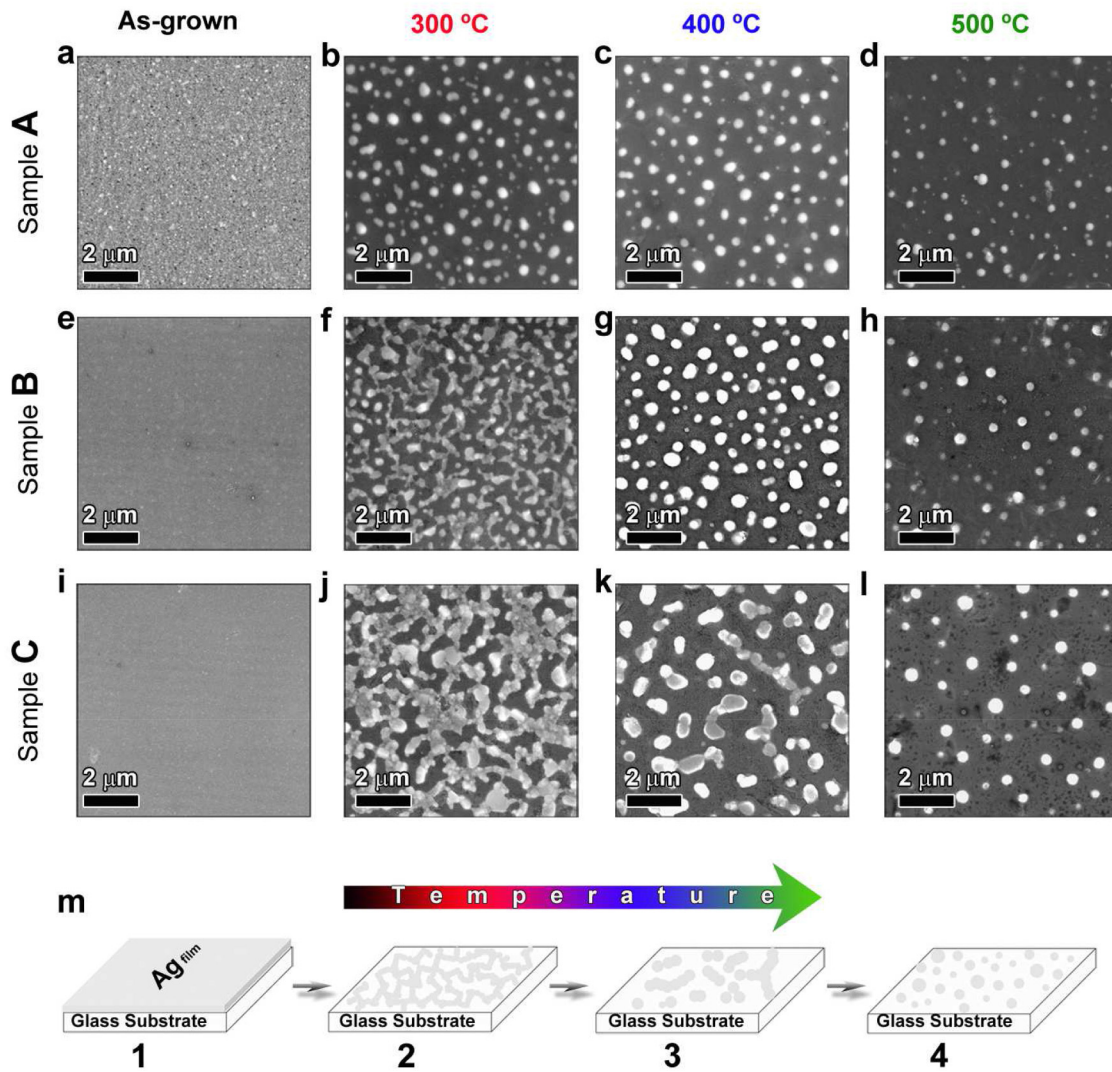


FIG. 1. [(a)–(l)] SEM images of Ag thin films deposited onto sodalime substrates and annealed at different temperatures in air for three different initial thicknesses. (m) Schematic representation of the solid-state dewetting mechanism for a Ag film increasing the annealing temperature (1 → 4).

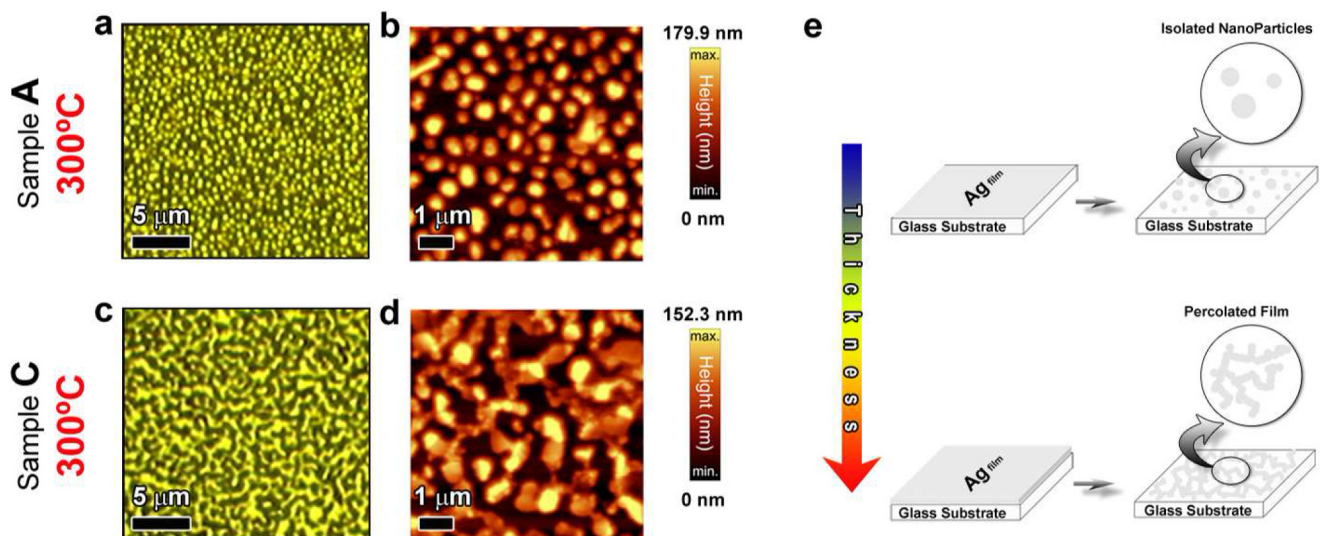


FIG. 2. [(a) and (c)] COM and [(b) and (d)] AFM topographic images of sample A (13 nm) and sample C (42 nm) deposited onto sodalime substrates and annealed at 300 °C in air. In COM images, bright green areas correspond to Ag, whereas dark areas correspond to the substrate. (e) Illustrative scheme showing the film thickness influence on the solid-state dewetting process for a Ag film.

nucleate and percolate leading to the formation of small islands with limited size and height as Fig. 3 evidences. The most significant parameter for the size and the height of Ag islands is the film initial thickness. Regarding the fraction of covered surface and the catchment area ($\sim d^2$, with d being the mean inter-island distance),^{21,34} these parameters depend mainly on the annealing temperature and do not depend so significantly on the Ag initial film thickness (see Fig. 3).

Comparing these values with those reported for Au film with similar thickness range, we find an analogous trend but with some significant differences, considering the discrepancy in the annealing time for the preparation of both sets of samples. In the previous work, Au films were annealed for 3 h, while, here, Ag films were treated for 10 min, since longer annealing times (hours) promoted Ag removal from the substrate. In the case of Ag films, we find that the island size strongly decreases with the annealing temperature [Fig. 3(a)], while for Au film with similar thickness, the island size showed a moderated increase. Moreover, considering the island average height, the uncovered area, and the catchment area, all three features are larger for Ag than for Au films.

This behavior can be ascribed to the difference in thermal expansion coefficient (Au: $14.2 \times 10^{-6} \text{ K}^{-1}$, Ag: $19.5 \times 10^{-6} \text{ K}^{-1}$, and sodalime: $7.5 \times 10^{-6} \text{ K}^{-1}$),^{35,36} the activation energy between Ag and Au on glass substrate for the process of surface diffusion, and the sublimation processes. The values of activation energy reported for Ag on SiO_2 are higher than those for Au on SiO_2 ,^{37,38} indicating that under the same conditions the process leads to the formation of a smaller number of holes and consequently larger catchment areas for the case of Ag films annealed even for smaller annealing time (note that the annealing time for Ag films was reduced to be 10 min instead of 3 h in the case of Au²¹). In the morphological evolution of nanostructures, the sublimation effect should be considered. Its rate depends on the equilibrium vapor pressure, the annealing temperature, and the molecular weight,²⁰ resulting in a larger atoms loss at higher temperature with the consequent decrease of island size, density, and larger catchment areas for the case of Ag.

Another indicator of this is the difference in the thermal expansion coefficients between film and substrate. In any case, Ostwald's ripening during the morphological evolution of nanostructures cannot be discarded.

In addition, the Ag oxidation that is discussed below may alter the kinetics of the process and consequently the morphology and physical properties of final nanostructures. The effect of sample oxidation depends on surface to volume ratio of Ag nanostructures and the annealing conditions (e.g., time and temperature), which has been evaluated by CRM. In the case of as-grown thin films, no Raman signal related to Ag oxide was detected from the mapping of several regions on samples. This result indicates a not significant oxidation of the films (under the resolution limit of the experimental system) in ambient air and/or during the Raman measurements by the laser source. On samples annealed at 300, 400, and 500 °C, Raman spectra (Fig. 4 for sample C) exhibit a band around 240 cm^{-1} attributed to the AgO formed during the annealing process and that corresponds to one of the stretching modes of Ag and O.^{25,39,40} However, the Raman intensity of this vibrational mode was found to be different depending on the location on the samples.

The oxidation level in Ag NPs was evaluated analyzing false color images from the mapping areas on sample surface. Integrating the elastic scattering band of laser source at 0 cm^{-1} for each spectrum collected, in-plane intensity Raman images [Fig. 4(b) for sample C annealed at 400 °C] show regions in which the elastic scattering band is higher corresponding to the more intense areas on optical image [see Fig. 4(a)] related to Ag NPs. Constructing a false color image with this signal and that related to the Raman band around 240 cm^{-1} associated with AgO [see Fig. 4(c)], we can observe that the oxidation signal is greater surrounding the Ag NPs. However, although less intense, the Raman band related to the AgO is also found on top of the Ag NPs. Due to the spherical geometry of NPs, the effective thickness of AgO at 2D projection of the NPs is higher on perimeter than on center. Hence, we can consider that a Ag oxide layer covering the Ag NPs is formed at surface level during the

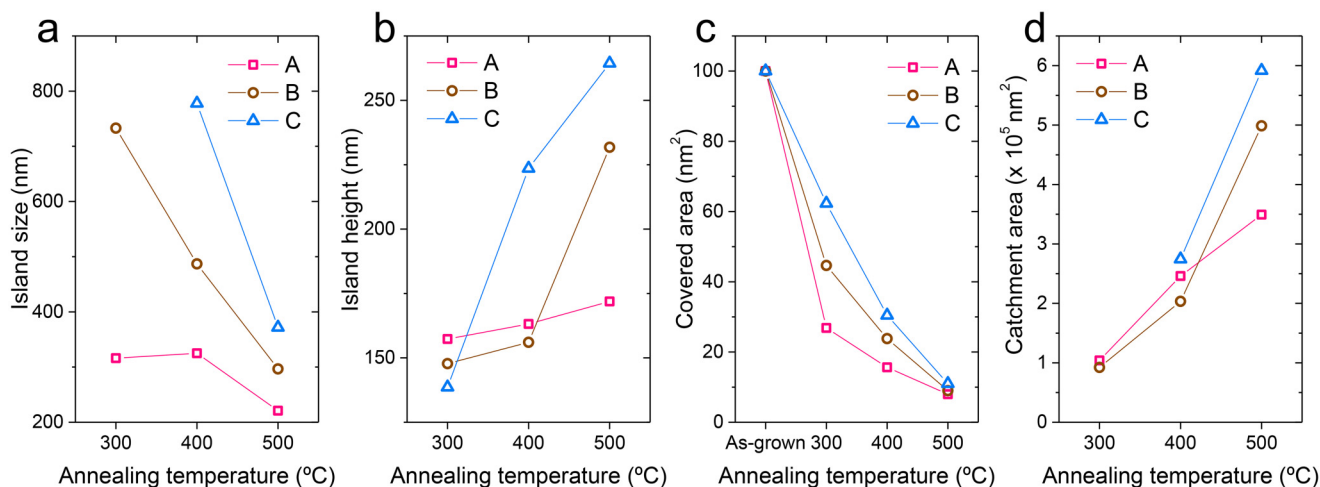


FIG. 3. Morphological parameters of Ag thin films as a function of initial film thickness and annealing temperature: (a) island size, (b) island height, (c) covered area, and (d) catchment area. Results have been derived from SEM and AFM images.

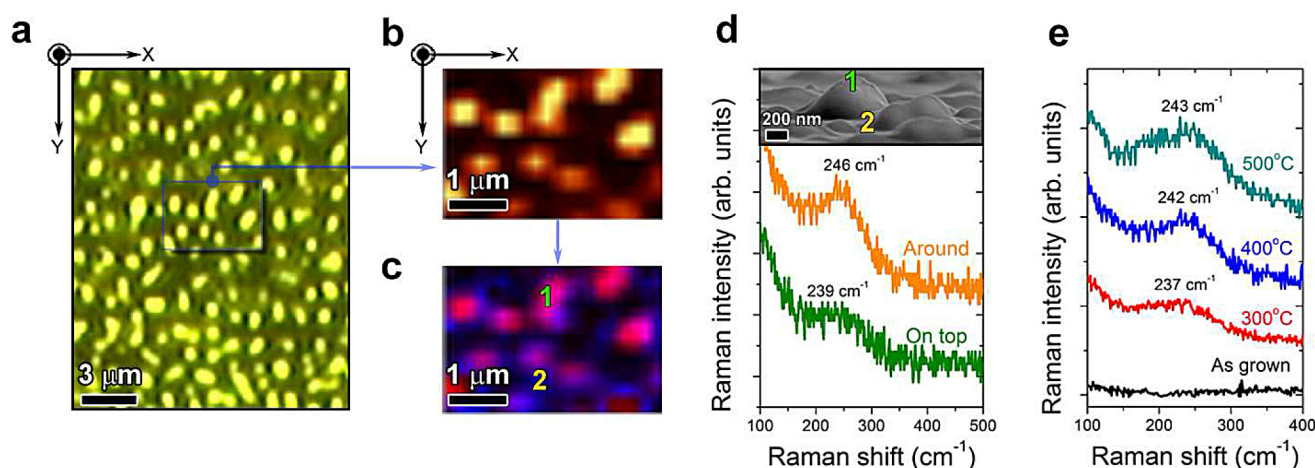


FIG. 4. (a) COM image of sample C (42 nm) deposited onto sodalime substrate and annealed at 400 °C in air. (b) XY Raman intensity image integrating the elastic scattering and (c) integrating the elastic scattering (red color) and the Raman band around 240 cm^{-1} related to AgO (blue color), from mapping the region marked with a blue square on COM image. (d) Raman spectra of 2 points marked on Raman image c and on tilted SEM image in the inset, showing the different Raman signal on top and around the Ag NPs. (e) Raman spectra of sample C (42 nm) in film form and annealed at different temperatures.

annealing process, as already reported by Pal *et al.*,²⁵ resulting in a passivation oxide layer that protects the metallic core of the NPs and giving place to core-shell Ag-AgO nanostructures.

As expected, the higher the annealing temperature, the higher the degree of oxidation of the samples. As Fig. 4(e) presents for sample C, a higher annealing temperature drives a more intense and a shift toward larger wavenumbers of the Raman band associated with the formation of AgO and so a larger degree of oxidation of Ag NPs. For samples varying the initial thickness, the Raman results were similar qualitatively.

B. Optical properties

Optical measurements evidenced a progressive transition from extended to localized surface plasmon in the samples as the process of nanostructuration takes place. Here, we evaluate the plasmonic evolution from the continuous Ag thin

films to Ag-AgO nanostructured systems, which has not been previously reported.

ESPR curves of the different samples are presented in Fig. 5. As-grown samples exhibit a SPR curve in agreement with the spectra calculated for Ag film with similar thicknesses (see Figs. 5 and 6). As the thickness of Ag film increases, ESPR curve becomes narrower and it shifted toward lower incident angles. The resonance is maximum for the as-grown sample C with attenuation over 90% of the incident light intensity. As the film becomes thinner, the destructive interference between the incident and backscattered beam induces a more significant damping of the ESPR leading to wider and weaker attenuation peaks. Mismatches between calculated and measured ESPR curves (i.e., resonant curve intensity and/or widening) can be associated with damping effects due to the surface roughness of the Ag films.^{2,21,22}

Abrupt changes in the resonant curves are detected for annealed samples with respect to the as-grown samples: the

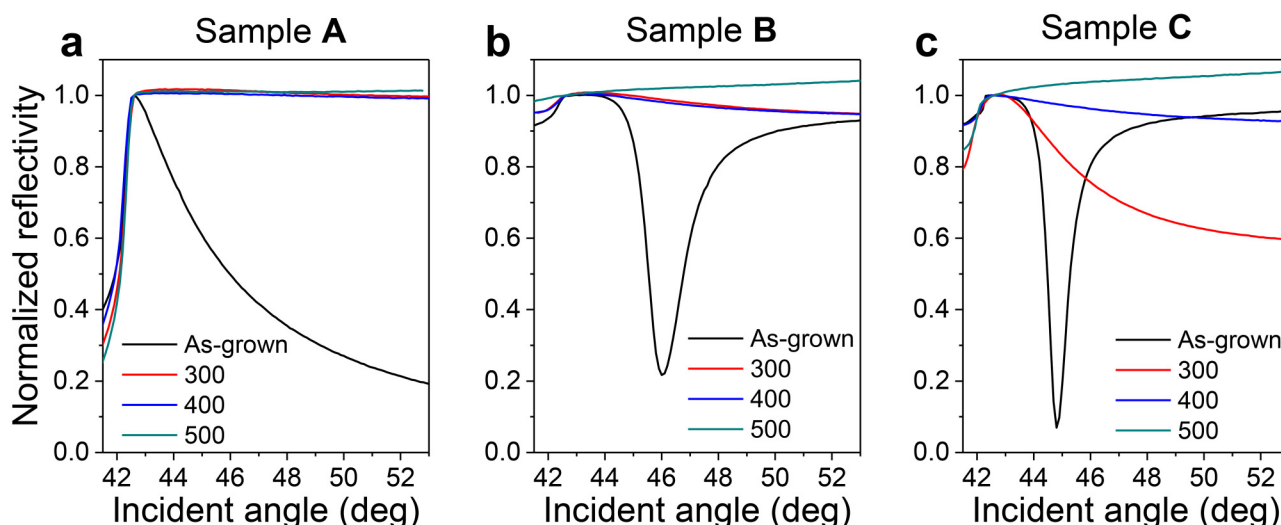


FIG. 5. ESPR curves measured in the ATR mode (Kretschmann-Raether configuration) for the Ag films (a) A (13 nm), (b) B (32 nm), and (c) C (42 nm), as-grown and annealed at different temperatures.

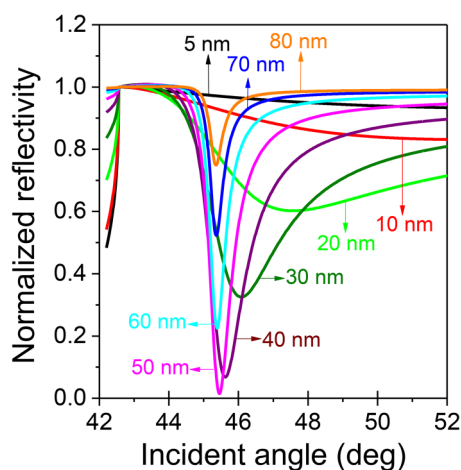


FIG. 6. Calculated ESR spectra for Ag films ($\epsilon_1 = -18.295$ and $\epsilon_2 = 0.48085$, according to Johnson and Christy²⁸ at $\lambda = 633$ nm) on glass substrate varying film thickness (5–80 nm).

larger the annealing temperature, the more pronounced the decrease of the SPR intensity and the wider the SPR resonance curve. These results agree with morphological analysis (see Figs. 1 and 2). ESR band is observed only for sample C annealed at 300 °C that exhibits the most continuous structure, while resonant curve is almost inappreciable or not observed for the case of annealed samples with isolated nanostructures exhibiting dimensions smaller than ESR wavelength.

As mentioned above, annealed samples are partially oxidized to AgO during the annealing treatment, which alters the SPR features. The dielectric constant of AgO is 6.25,⁴¹ larger than that of air. This effect may be noted in the ESR curves, giving rise to an *extra* shift of the SPR toward larger angles and a wider and weaker SPR resonance curve.^{2,22}

Figure 7 presents optical absorption spectra of samples evaluated in this work. In addition to the optical absorption features of Ag, we identify an absorption edge at about 320 nm due to the sodalime substrate. As-grown samples exhibit the

typical spectra for Ag thin films,⁴² while optical absorption of annealed Ag films depends on the morphological and structural features of final nanostructures. The main effect of the annealing process is the decrease of the absorption coefficient in the whole spectral range. This drastic alteration is due to the formation of holes during annealing, providing pathways of light that cross without interacting with the Ag nanostructures. Such an effect is larger as the annealing temperature increases.

The typical absorption band of Ag NPs (i.e., LSPR) is clearly observed for samples annealed with a discrete structure and whose characteristics depend on the temperature during the annealing process and the initial film thickness. The LSPR band for sample A annealed at 300 °C is observed at about 430 nm and shifted toward larger wavelengths with respect to the expected position for metallic Ag NPs.²² These shifts are induced by the presence of AgO with a larger dielectric permittivity surrounding the Ag nanostructures. Larger abundance of AgO prompts a larger shift of the LSPR position^{43,44} in those samples with a discrete structure. Concerning the intensity of the LSPR band, samples B and C annealed at 500 °C exhibit the most intense resonance. This effect is due to the larger presence of isolated and rounded NPs with dimensions fairly smaller than the excitation wavelength of SPs. For samples with larger initial film thickness (samples B and C) and annealed at lower temperature, a magnified view of spectra is necessary for revealing a weak and wide absorption band due to the presence of Ag nanostructures exhibiting a wide distribution of morphologies.

All samples revealing LSPs exhibit a blue-shift and narrowing of the absorption band as the annealing temperature increases, which can be clearly seen in the inset of Fig. 7(a) for sample A, and this is related to variations in the shape and inter-particle distance.^{21,44,45} LSPR band is more similar to that expected for isolated Ag NPs in the case of films annealed at higher temperatures (500 °C), where the distance between particles is larger and they exhibit a more rounded shape (see Fig. 1).

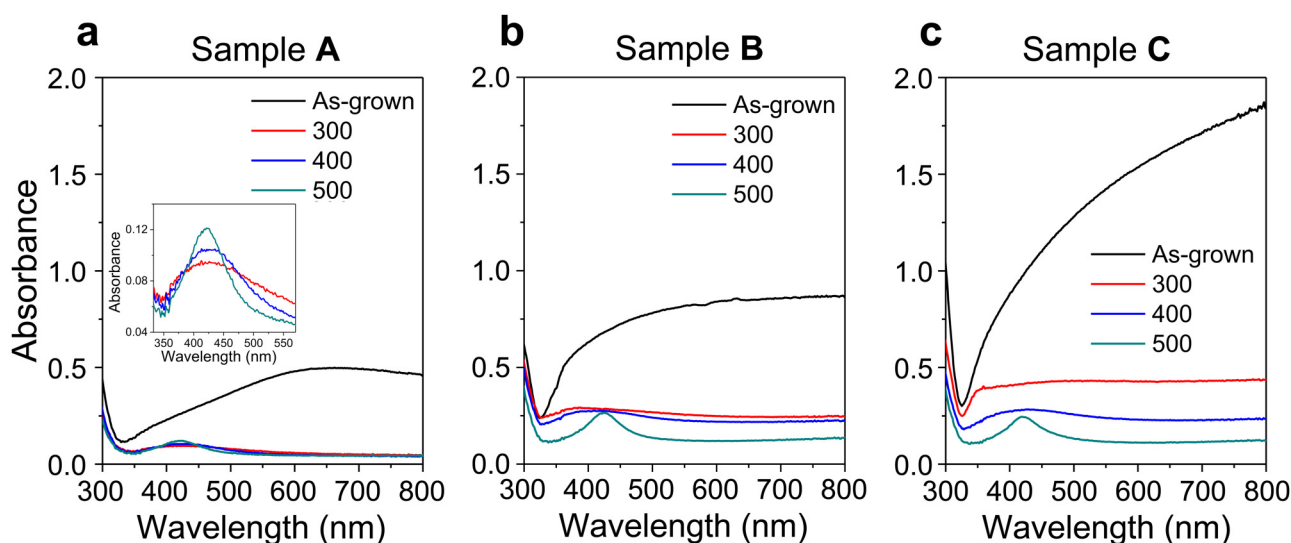


FIG. 7. Optical absorption spectra for the Ag films (a) A (13 nm), (b) B (32 nm), and (c) C (42 nm), as-grown and after annealing at different temperatures.

Finally, besides the well-defined stages where SPs with localized and extended character can be excited, we notice a point of crossing where both LSPs and ESPs may coexist, similar to our previous work in Au films.²¹ For as-grown sample A, the clear plateau extended up to the NIR region in the optical absorption spectrum and the increase in the intensity of the ESPR curve designates that amazing region for the plasmonic applications.

IV. CONCLUSIONS

Ag thin films have been grown on sodalime glass substrates and subsequently annealed in air at different temperatures (300–500 °C). The thermal treatment promotes the morphological modification of the thin films leading to a nanostructured layer plus a partial oxidation of the Ag nanostructures. The island size, shape, height, inter-island distance, and the oxidation level of Ag-AgO nanoparticles depend on the initial film thickness and annealing temperature. Optical response is quantitatively and qualitatively altered by the morphological and structural modifications induced by the annealing process of Ag films, and the plasmonic transitions have been presented. Thus, annealing of Ag films allows progressively tuning the optical properties of Ag films on glasses from ESPR to LSPR and their range of applications.

ACKNOWLEDGMENTS

This work has been supported by the Ministerio Español de Economía, Industria y Competitividad (MINECO) through the Project Nos. MAT2017-86540-C4-1-R, MAT2013-48009-C4-1-P, and FIS-2008-06249. Project supported by a 2016 BBVA Foundation Grant for Researchers and Cultural Creators. F. R-M. is also indebted to MINECO for a “Ramon y Cajal” contract (Ref: RyC-2015-18626), which is co-financed by the European Social Fund.

- ¹A. Rizzo, M. A. Tagliente, M. Alvisi, and S. Scaglione, *Thin Solid Films* **396**, 29 (2001).
- ²H. Raether, *Surface Plasmons on Smooth and Rough Surfaces and on Gratings* (Springer-Verlag, Berlin, 1988).
- ³M. Mirzaei, A. A. Ogwu, H. F. Jirandehi, S. Aidarova, Z. Ospanova, and N. Tsendzughul, *Colloids Surf. A Physicochem. Eng. Asp.* **519**, 223 (2017).
- ⁴H. A. Atwater and A. Polman, *Nat. Mater.* **9**, 205 (2010).
- ⁵S. Pillai, K. R. Catchpole, T. Trupke, and M. A. Green, *J. Appl. Phys.* **101**, 093105 (2007).
- ⁶W. Fritzsche and T. A. Taton, *Nanotechnology* **14**, R63 (2003).
- ⁷M. Rycenga, P. H. C. Camargo, W. Li, C. H. Moran, and Y. Xia, *J. Phys. Chem. Lett.* **1**, 696 (2010).
- ⁸C. H. Kwon, D. W. Boo, H. J. Hwang, and M. S. Kim, *J. Phys. Chem. B* **103**, 9610 (1999).
- ⁹W. H. Hung, M. Aykol, D. Valley, W. Hou, and S. B. Cronin, *Nano Lett.* **10**, 1314 (2010).

- ¹⁰E. M. Larsson, C. Langhammer, I. Zorić, and B. Kasemo, *Science* **326**, 1091 (2009).
- ¹¹S. Shrivastava, T. Bera, A. Roy, G. Singh, P. Ramachandrarao, and D. Dash, *Nanotechnology* **18**, 225103 (2007).
- ¹²G. A. Sotiriou and S. E. Pratsinis, *Curr. Opin. Chem. Eng.* **1**, 3 (2011).
- ¹³X. Li, W. C. H. Choy, X. Ren, D. Zhang, and H. Lu, *Adv. Funct. Mater.* **24**, 3114 (2014).
- ¹⁴X. Li, X. Ren, Y. Zhang, W. C. H. Choy, and B. Wei, *Nanoscale* **7**, 11291 (2015).
- ¹⁵C. V. Thompson, *Annu. Rev. Mater. Res.* **42**, 399 (2012).
- ¹⁶F. Leroy, L. Borowik, F. Cheynis, Y. Almadori, S. Curietto, M. Trautmann, J. C. Barbe, and P. Müller, *Surf. Sci. Rep.* **71**, 391 (2016).
- ¹⁷P. Jacquet, R. Podor, J. Ravoux, J. Teisseire, I. Gozhyk, J. Jupille, and R. Lazzari, *Scr. Mater.* **115**, 128 (2016).
- ¹⁸N. J. Simrick, J. A. Kilner, and A. Atkinson, *Thin Solid Films* **520**, 2855 (2012).
- ¹⁹S. Kunwar, M. Li, P. Pandey, M. Sui, Q. Zhang, and J. Lee, *Mater. Res. Express* **3**, 125006 (2016).
- ²⁰P. Pandey, S. Kunwar, M. Sui, M. Y. Li, Q. Zhang, and J. Lee, *Phys. Status Solidi Appl. Mater. Sci.* **214**, 1600702 (2017).
- ²¹A. Serrano, O. Rodríguez de la Fuente, and M. A. García, *J. Appl. Phys.* **108**, 74303 (2010).
- ²²A. Serrano, *Modified Au-Based Nanomaterials Studied by Surface Plasmon Resonance Spectroscopy* (Springer Theses, 2015).
- ²³M. Sui, P. Pandey, S. Kunwar, M. Y. Li, Q. Zhang, and J. Lee, *Superlattices Microstruct.* **100**, 1128 (2016).
- ²⁴J. Quan, J. Zhang, X. Qi, J. Li, N. Wang, and Y. Zhu, *Sci. Rep.* **7**, 14771 (2017).
- ²⁵A. K. Pal and D. Bharathi Mohan, *Opt. Mater. (Amst.)* **48**, 121 (2015).
- ²⁶R. P. Van Duyne, J. C. Hulst, and D. A. Treichel, *J. Chem. Phys.* **99**, 2101 (1993).
- ²⁷See <http://www.mpip-mainz.mpg.de/knoll/soft>. We simulated the spectra with the WINSPALL freeware code, (n.d.).
- ²⁸P. B. Johnson and R. W. Christy, *Phys. Rev. B* **6**, 4370 (1972).
- ²⁹A. Araújo, M. J. Mendes, T. Mateus, A. Vicente, D. Nunes, T. Calmeiro, E. Fortunato, H. Águas, and R. Martins, *J. Phys. Chem. C* **120**, 18235 (2016).
- ³⁰A. E. B. Presland, G. L. Price, and D. L. Trimm, *Surf. Sci.* **29**, 424 (1972).
- ³¹R. Bernardo-Gavito, A. Serrano, M. A. García, R. Miranda, and D. Granados, *J. Appl. Phys.* **114**, 164312 (2013).
- ³²S. Morawiec, M. J. Mendes, S. Mirabella, F. Simone, F. Priolo, and I. Crupi, *Nanotechnology* **24**, (2013).
- ³³S. K. Sharma and J. Spitz, *Thin Solid Films* **65**, 339 (1980).
- ³⁴M. S. Rahman Khan, *Bull. Mater. Sci.* **9**, 55 (1987).
- ³⁵J. A. Thornton and D. W. Hoffman, *Thin Solid Films* **171**, 5 (1989).
- ³⁶Y. S. Touloukian, R. K. Kirby, R. E. Taylor, and P. D. Desai, *Thermal Expansion: Metallic Elements and Alloys (Thermophysical Properties of Matter)*, 1st ed. (IFI/Plenum, 1975), Vol. 12.
- ³⁷J. H. Kim and P. J. Moyer, *Opt. Express* **14**, 6595 (2006).
- ³⁸A. D. LaLonde, M. G. Norton, D. Q. Zhang, D. Gangadean, A. Alkhateeb, R. Padmanabhan, and D. N. McIlroy, *J. Mater. Res.* **20**, 3021 (2005).
- ³⁹J. Lv, F. Lai, L. Lin, Y. Lin, Z. Huang, and R. Chen, *Appl. Surf. Sci.* **253**, 7036 (2007).
- ⁴⁰Y. Zhao, Y. Xie, Y. Y. Hui, L. Tang, W. Jie, Y. Jiang, L. Xu, S. P. Lau, and Y. Chai, *J. Mater. Chem. C* **1**, 4956 (2013).
- ⁴¹T. V. Shahbazyan and M. I. Stockman, *Plasmonics: Theory and Applications* (Springer Science & Business Media, 2014).
- ⁴²J. Gong, R. Dai, Z. Wang, and Z. Zhang, *Sci. Rep.* **5**, 9279 (2015).
- ⁴³A. Kuzma, M. Weis, S. Flickyngeroova, J. Jakabovic, A. Satka, E. Dobrocka, J. Chlpik, J. Cirak, M. Donoval, P. Telek, F. Uherek, and D. Donoval, *J. Appl. Phys.* **112** (2012).
- ⁴⁴U. Kreibitz and M. Vollmer, *Optical Properties of Metal Clusters, Springer Series in Material Science* (Springer-Verlag, Berlin, 1995).
- ⁴⁵M. A. Garcia, *J. Phys. D. Appl. Phys.* **44**, 283001 (2011).